INTERNATIONAL JOURNAL FOR NUMERICAL METHODS IN FLUIDS
Int. J. Numer. Meth. Fluids 2009; **60**:893–918
Published online 17 September 2008 in Wiley InterScience (www.interscience.wiley.com). DOI: 10.1002/fld.1924

A new interface-capturing discretization scheme for numerical solution of the volume fraction equation in two-phase flows

D. Keith Walters*,†,‡ and Nicole M. Wolgemuth§

Department of Mechanical Engineering, HPC² SimCenter, Mississippi State University, Mississippi State, MS 39762, U.S.A.

SUMMARY

A new high-resolution spatial discretization scheme for use with the interface-capturing volume-of-fluid method is presented and applied to several test cases. The new scheme is intended to preserve the volume fraction discontinuity without the need to explicitly reconstruct the interface within computational control volumes near the interface. The method is based on maximization of the volume fraction gradient in the region of the interface, while stability is preserved by maintaining net upwind biasing of the face flux prescription in each computational control volume. In addition, the scheme employs face limiting to satisfy boundedness criteria at finite-volume control surfaces (faces) and prevent variable overshoot. The method has been developed for use with unstructured, anisotropic, and/or inhomogeneous meshes that are often used for simulation of geometrically complex flow fields. This paper presents the implementation of the new discretization scheme into a steady-state solver in order to isolate the spatial discretization from the time integration technique. The new scheme is validated for steady-state two-phase flow using several test cases, and is shown to preserve the phase interface almost exactly, with essentially zero dissipative or dispersive error in the volume fraction solution. Copyright © 2008 John Wiley & Sons, Ltd.

Received 8 January 2007; Revised 5 August 2008; Accepted 8 August 2008

KEY WORDS: CFD; two phase; discretization; interface capturing; algorithms; flow

1. INTRODUCTION

Multi-phase finite-volume computational fluid dynamics (CFD) simulations include both surface-capturing and surface-tracking approaches. The former often utilizes the volume-of-fluid (VOF)

*Correspondence to: D. Keith Walters, Department of Mechanical Engineering, HPC² SimCenter, P.O. Box ME, Mississippi State University, Mississippi State, MS 39762, U.S.A.
†E-mail: walters@me.msstate.edu
‡Assistant Professor.
§Undergraduate Student Researcher.

Contract/grant sponsor: National Science Foundation; contract/grant number: EPS-0556308

method [1] to resolve the separation of phases. Here 'volume-of-fluid method' refers to Eulerian computation of multi-phase flow via the incorporation of an additional volume fraction equation for each additional phase beyond the primary, independent of the details of the discretization scheme. Fluid properties are computed within each control volume based on the volume fraction of each phase, using an appropriate mixture rule. The governing continuity, momentum, and energy equations are then solved for a single set of shared flow variables (velocity, pressure, etc.). The numerical solution of these equations can be obtained using any appropriate method for single-phase incompressible or compressible flow.

Numerical solution of the volume fraction equation requires a discretization scheme that is capable of resolving the sharp discontinuity between phases. Two general classifications of discretization are interface reconstruction and interface capturing. Interface reconstruction methods attempt to explicitly approximate the location of the phase interface within computational control volumes (cells) based on the volume fraction values in cells near the interface. Several methods have been documented in the open literature, including the simple line interface calculation scheme [2] and the piecewise linear interface calculation scheme [3]. Numerical solution consists of two steps: reconstruction of the interface approximation to compute face fluxes, and numerical integration of the volume fraction equation. These methods employ unsteady (time-dependent) numerical schemes, and steady-state solutions are obtained by integrating for sufficiently long times.

By contrast, interface-capturing methods rely on a high-resolution discretization scheme to resolve the volume fraction distribution, without any attempt to explicitly reconstruct the exact location of the interface. Recently proposed schemes are based on the normalized variable diagram (NVD) [4] and have been constructed for use with both structured and unstructured meshes [5–7]. For example, one such method is the high-resolution interface-capturing (HRIC) scheme of Muzaferija *et al.* [5], which has been shown to be a relatively accurate and computationally efficient approach to VOF simulations of steady and unsteady free-surface problems [8, 9]. One advantage of the interface-capturing approach is that it does not require any additional reconstruction steps during the solution process, and the volume fraction equation is solved in a manner consistent with the other governing equations. In addition, the interface-capturing method can be implemented in either a steady-state or an unsteady formulation, using implicit solution techniques. It is therefore more easily integrated into existing single-phase CFD solvers.

This paper presents a new high-resolution discretization scheme for use with the interface-capturing approach to VOF simulations. The method is based on maximization of the volume fraction gradient in the region of the discontinuity, and is easily incorporated on both structured and unstructured meshes. The goal of the present work is to present the method formulation, and to demonstrate its performance in terms of preserving the volume fraction discontinuity with a minimum amount of dissipative error. The test cases considered herein are steady state and non-turbulent, in order to isolate the performance of the spatial discretization, independent of the time integration technique and turbulence model.

The remainder of this paper is organized as follows. The next section presents the governing equations and the general numerical method. The succeeding section then presents the details of the new discretization scheme. The new scheme is then applied to several simple demonstration cases to show its capability to preserve discontinuities using either structured Cartesian or unstructured meshes. Results are then presented for realistic two-phase flow test cases, and compared with experimental data and with results obtained using currently available schemes. The final section draws conclusions and summarizes future work.

DOI: 10.1002/fld

2. NUMERICAL METHOD

We consider the general case of a two-phase fluid mixture in which each of the phases is incompressible. The system is governed by the continuity and momentum (Navier–Stokes) equations. For steady, laminar flow

$$\frac{\partial u_j}{\partial x_j} = 0 \tag{1}$$

$$\frac{\partial (u_i u_j)}{\partial x_j} = -\frac{1}{\rho}\frac{\partial P}{\partial x_i} + \frac{\partial}{\partial x_j}\left[\frac{\mu}{\rho}\left(\frac{\partial u_i}{\partial x_j} + \frac{\partial u_j}{\partial x_i}\right)\right] + g_i \tag{2}$$

In the VOF approach, an additional equation is solved for the volume fraction of the secondary phase (discussed in the following section) and the properties in Equations (1) and (2) are computed based on of the local secondary phase volume fraction, α, as

$$\rho = \alpha\rho_1 + (1-\alpha)\rho_0 \tag{3}$$

$$\mu = \alpha\mu_1 + (1-\alpha)\mu_0 \tag{4}$$

Here the subscripts 0 and 1 refer to the (constant-valued) properties of the primary and secondary phases, respectively.

The finite-volume method for solution of the coupled continuity and momentum equations requires integration of the equations over finite computational control volumes, or cells, representing the physical discretization (mesh) of the overall flow domain. Discrete forms of the governing equations are developed by approximating the surface fluxes at the bounding faces of each cell. The flux approximations are determined by the choice of spatial discretization scheme. Several well-known schemes are available for incompressible flow. The focus of the present study is on the solution of the volume fraction equation, but the remaining numerical details are briefly outlined in the following paragraph.

Note that the governing equations do not include surface tension terms. Surface tension effects are considered negligible for all test cases considered here, as the focus of the current paper is strictly on minimizing dissipative error in the volume fraction equation. It should be noted that inclusion of surface tension forces in the momentum equation often produces error in the form of parasitic currents in the velocity field. Whereas the volume fraction discretization scheme presented here is not expected to mitigate these errors, future research efforts will seek to address this issue.

All of the results in this paper were obtained using the FLUENT solver, version 6.2.16, from Fluent Inc. With the exception of the newly developed volume fraction discretization scheme, all of the numerical details represent options currently available in the FLUENT solver. The simulations were performed using a steady-state, segregated, implicit scheme. The pressure and velocity fields were coupled using the SIMPLE algorithm [10]. The face values of pressure were obtained using the PRESTO! scheme [11], which is based on the use of a staggered control volume surrounding mesh faces, analogous to the staggered-grid schemes used on structured meshes [10]. The spatial discretization for the convective terms in the momentum equations was accomplished using a second-order upwind scheme [12]. These algorithmic details represent a current standard for computation of steady-state incompressible flow, and are similar to those used in other VOF simulations that have recently been documented in the literature (cf. [13–16]).

DOI: 10.1002/fld

3. DISCRETIZATION OF THE VOLUME FRACTION EQUATION

3.1. Background

In the VOF method, the equation governing the volume fraction for secondary phase q, α_q, can be expressed in general form as

$$\frac{\partial(\rho_q \alpha_q)}{\partial t} + \frac{\partial(\rho_q u_j \alpha_q)}{\partial x_j} = S_q \tag{5}$$

where ρ_q is the density of phase q, and u_i is the velocity, which is shared by all phases. The source term S_q represents mass exchange between phases. For simplified discussion of the numerical scheme, we consider only one secondary phase, constant density within each phase, and no mass exchange. In addition, we consider only the steady-state case, as the present work focuses on the spatial discretization scheme. The simplified form of the equation is

$$\frac{\partial(u_j \alpha)}{\partial x_j} = 0 \tag{6}$$

As discussed above, the finite-volume numerical approach is based on physical discretization of the domain of interest into a number of finite control volumes (cells) of domain Ω, and integration of the governing equation over each control volume

$$\int_{\mathrm{d}\Omega} u_j \alpha n_j \, \mathrm{d}A = 0 \tag{7}$$

where n_j is the outward-pointing normal vector on the control volume surface. The surface integration is typically computed by a discrete sum over each of the bounding faces of the computational cell

$$\int_{\mathrm{d}\Omega} u_j \alpha n_j \, \mathrm{d}A \approx \sum_{\#\ \text{faces}} (\mathbf{u}_f \cdot \mathbf{n}_f) \alpha_f A_f \approx \sum_{\#\ \text{faces}} \dot{Q}_f \alpha_f \tag{8}$$

Here the f subscript is the control volume face index, A is the face area, and the simplified notation $\dot{Q}_f$ is adopted to denote the volumetric flow rate across each face, as indicated in Figure 1. Also shown is the definition of cell neighbors for a given face as either upstream or downstream, depending on the local velocity direction. In a similar manner, the faces bounding each cell can be denoted as upstream (relative to the cell) when the volumetric flow rate $\dot{Q}_f$ is negative (into the cell) and downstream when $\dot{Q}_f$ is positive (out of the cell). For purposes of numerical discretization, the significance of upstream and downstream mesh quantities is well understood. Flow field information is carried along the characteristics in the downstream direction by the advective terms in the governing equation. As a consequence, increasing the relative strength of the contribution of upwind cell states to face flux calculations (upwind biasing) results in increased stability of the numerical scheme. For multi-dimensional problems, however, upwind biasing also tends to introduce dissipation error into the scheme [10].

In general, the spatial discretization scheme expresses the face value α_f in terms of local cell-averaged values. For example, one form of the central-difference scheme expresses α_f as an average of the upstream and downstream cell values

$$\alpha_f = \tfrac{1}{2}(\alpha_{\mathrm{U}} + \alpha_{\mathrm{D}}) \tag{9}$$

DOI: 10.1002/fld

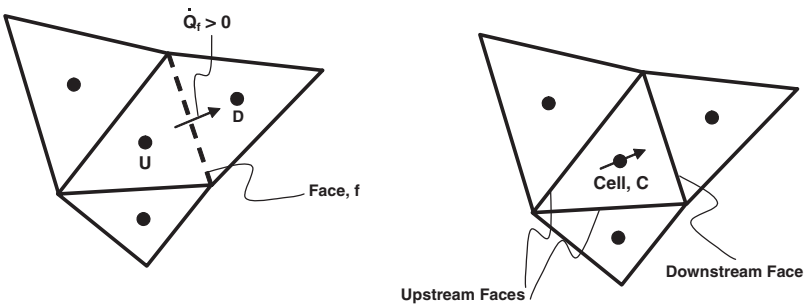

Figure 1. Illustration of 2-D unstructured mesh summarizing finite-volume discretization technique, including definitions of: (a) upstream and downstream cell neighbors and (b) upstream and downstream faces for a given cell.

This scheme is generally unstable; an alternative is the first-order upwind scheme

$$\alpha_f = \alpha_{\mathrm{U}} \tag{10}$$

This formulation is stable but produces unacceptably high levels of numerical dissipation, making it impractical for use in VOF simulations. Several alternative higher-order upwind-biased methods have been proposed [4], for example the upwind-biased reconstruction method adopted from Barth and Jespersen [12]:

$$\alpha_f = \alpha_{\mathrm{U}} + (\nabla\alpha)_{\mathrm{U}} \cdot (\bar{x}_f - \bar{x}_{\mathrm{U}}) \tag{11}$$

where $(\nabla\alpha)_{\mathrm{U}}$ is the gradient evaluated in the upstream cell neighbor. The gradient is typically limited to prevent face maxima or minima.

More recently, HRIC discretization schemes [5–7] have been proposed for use with the VOF method. For example, the HRIC scheme of Muzaferija *et al.* [5] is a composite NVD scheme based on donor, acceptor, and upwind cells. On Cartesian meshes, the definition of each is clearly defined. On unstructured meshes, the upwind cell is replaced by a value extrapolated from the donor cell using the locally computed variable gradient. In terms of the nomenclature outlined in Figure 1, the donor and acceptor cells correspond to the upstream and downstream cells, and the extrapolated upwind cell (on unstructured meshes) is denoted by the symbol UU, as shown in Figure 2. To implement the HRIC scheme, a normalized cell volume fraction is first calculated for the upstream cell as

$$\alpha'_{\mathrm{U}} = \frac{\alpha_{\mathrm{U}} - \alpha_{\mathrm{UU}}}{\alpha_{\mathrm{D}} - \alpha_{\mathrm{UU}}} \tag{12}$$

The normalized volume fraction at the face lying between the upstream and downstream (donor and acceptor) cells is computed by

$$\alpha'_{f,\mathrm{HRIC}} = \begin{cases} \alpha'_{\mathrm{U}}, & \alpha'_{\mathrm{U}} < 0 \text{ or } \alpha'_{\mathrm{U}} > 1 \\ 2\alpha'_{\mathrm{U}}, & 0 \leqslant \alpha'_{\mathrm{U}} \leqslant 0.5 \\ 1, & 0.5 \leqslant \alpha'_{\mathrm{U}} \leqslant 1 \end{cases} \tag{13}$$

DOI: 10.1002/fld

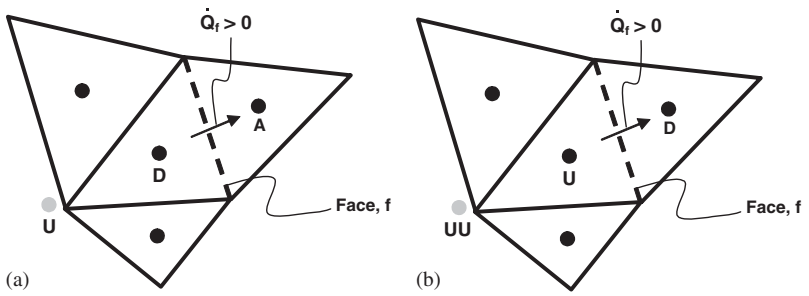

Figure 2. Comparison of 'donor–acceptor' versus current nomenclature. In (a), the value of the face f is determined by the upstream (U), donor (D), and acceptor (A) cells, which correspond to the projected (UU), upstream (U), and downstream (D) cells in part (b).

The version of the HRIC scheme used in this paper for comparison purposes is a modified form incorporated into the FLUENT flow solver. To avoid 'wrinkles' in the predicted interface path, the scheme switches to ULTIMATE QUICKEST [4] when the angle between the face normal and the interface normal becomes orthogonal. The value of the normalized face volume fraction for the ULTIMATE QUICKEST scheme is

$$\alpha'_{f,\mathrm{UQ}} = \begin{cases} \alpha'_{\mathrm{U}}, & \alpha'_{\mathrm{U}} < 0 \text{ or } \alpha'_{\mathrm{U}} > 1 \\ \mathrm{MIN}\left(\alpha'_{f,\mathrm{HRIC}}, \dfrac{6\alpha'_{\mathrm{U}}+3}{8}\right), & 0 \leqslant \alpha'_{\mathrm{U}} \leqslant 1 \end{cases} \tag{14}$$

The corrected value of the normalized volume fraction is a weighted average between the two values above

$$\alpha'_{f,\mathrm{CORR}} = \alpha'_{f,\mathrm{HRIC}}\sqrt{\cos\theta} + \alpha'_{f,\mathrm{UQ}}(1-\sqrt{\cos\theta}) \tag{15}$$

where θ represents the angle between the mesh face and the phase interface, and is estimated by

$$\cos\theta = \frac{\nabla\alpha\cdot\mathbf{d}}{|\nabla\alpha|\,|\mathbf{d}|} \tag{16}$$

The vector $\mathbf{d}$ connects the cell centers of the upstream and downstream cells. Finally, the face value of the volume fraction is computed from the normalized value as

$$\alpha_f = \alpha_{\mathrm{U}} + \alpha'_{f,\mathrm{CORR}}(\alpha_{\mathrm{D}} - \alpha_{\mathrm{UU}}) \tag{17}$$

The HRIC method outlined above is similar in form to other NVD-based schemes found in the open literature [2, 6, 7, 17]. All are characterized by downstream-weighted differencing (e.g. Equation (13)), in conjunction with a means of 'switching' to upwind differencing under certain flow conditions, i.e. when the face is oriented nearly orthogonal to the volume fraction interface. The goal of the present study is to introduce a downstream-weighted discretization scheme that more accurately preserves the interface, without the need for *ad hoc* 'switching', and without introducing non-physical oscillations ('wrinkles') in the computed interface.

DOI: 10.1002/fld

3.2. Bounded gradient maximization (BGM) scheme

The current study introduces a new discretization method as an alternative to currently used NVD-based schemes. The BGM scheme proposed here expresses the face value of the volume fraction as a linear combination of the upstream cell neighbor value and an extrapolated downstream face value. The goal of the discretization is to maximize the local volume fraction gradient by maximizing the degree to which the face value is weighted toward the extrapolated downstream value. It is well known that introducing a downwind component into the discretization tends to produce non-physical oscillations and, in the absence of appropriate limiters or artificial dissipation operators, can lead to instability. In contrast to previous methods, the current scheme adds an additional term to the face flux in order to provide a net upwinding component and ensure stability. Further, the face value of the volume fraction is limited to minimum and maximum values of zero and one, respectively.

The first step is to compute an initial approximation of face values by extrapolating from the upstream cell, using an expression similar to the second-order upwind scheme

$$\alpha_f^* = \alpha_U + (\nabla\alpha)_U \cdot (\bar{x}_f - \bar{x}_U) \tag{18}$$

Computation of the volume fraction gradient $\nabla\alpha$ is discussed in more detail below. The general expression for the volume fraction at each face is obtained from

$$\alpha_f = \alpha_U + W_U(\alpha_f^* - \alpha_U) + W_U\tilde{\alpha}_U \tag{19}$$

The variable parameter W assumes a value greater than or equal to zero (and may be greater than one) and is defined within each computational cell, so that the first two terms on the right-hand side of Equation (19) represent a linear weighted function between upstream and downstream values. It is apparent that, as $W \to 0$, the first-order upwind scheme (Equation (10)) is recovered. The additive term $W\tilde{\alpha}$ is included to help preserve the stability of the scheme for any value of W. Like W, the value of the corrective volume fraction $\tilde{\alpha}$ is computed within each cell, and is applied at each of the downstream faces bounding the cell. Stability is maintained when

$$\sum_{f:\dot{Q}_f>0} \dot{Q}_f \alpha_f = \sum_{f:\dot{Q}_f>0} \dot{Q}_f \alpha_U \tag{20}$$

Equation (20) is therefore a constraint based on summation over each of the downstream faces bounding a particular mesh cell. This constraint ensures that the total outward convective flux from the cell is equal to that for a first-order upwind scheme. Substitution of the face formulation (Equation (19)) into Equation (20) yields the following result, independent of W:

$$\tilde{\alpha}_U = \frac{\sum_{f:\dot{Q}_f>0} \dot{Q}_f(\alpha_U - \alpha_f^*)}{\sum_{f:\dot{Q}_f>0} \dot{Q}_f} \tag{21}$$

Computation of the additive term $\tilde{\alpha}$ within each cell in the domain is therefore carried out by summing over all downstream faces (i.e. faces for which volumetric flow rate is out of the cell) to obtain the terms in the numerator and denominator of Equation (21).

The limited value of the weight factor in each cell is then computed by determining the maximum value of W for which the following boundedness criteria are satisfied. First, for each

DOI: 10.1002/fld

of the downstream faces bounding a particular cell

$$0 \leqslant \alpha_f \leqslant 1 \tag{22}$$

This limiter is simply an expression of the physical bound on volume fraction, applied at each face in the domain. On 2-D and structured Cartesian meshes, this limiter appears sufficient to ensure stable and accurate behavior.

On 3-D unstructured or general topology meshes, an additional criterion is enforced to ensure accurate behavior of the scheme. The limiter expressed in Equation (22) is applied at 'shadow faces' projected downstream from the upwind faces of each grid cell. The shadow faces are illustrated in Figure 3 for a 2-D triangular cell. Each shadow face centroid is projected from the upstream face centroid through the cell centroid as shown, so that the vector connecting the cell and shadow face centroids is given by:

$$\bar{x}_{f,\text{shadow}} - \bar{x}_C = -(\bar{x}_{f,\text{upwind}} - \bar{x}_C) \tag{23}$$

The value of the volume fraction at each shadow face is computed from Equations (18) and (19), and the limiting constraint of Equation (22) is applied:

$$0 \leqslant \alpha_{f,\text{shadow}} \leqslant 1 \tag{24}$$

The limited value of W in each cell is obtained by taking the minimum constrained value computed for all downstream and shadow faces. This procedure is analogous to the gradient limiter used by Barth and Jespersen [12] to bound face values between cell neighbor values.

Care must be taken when approximating the volume fraction gradient term $\nabla\alpha$. On Cartesian structured meshes, the gradient may simply be computed using a discrete form of the so-called Green–Gauss theorem:

$$(\nabla\alpha)_C = \frac{1}{V_c} \sum_{\#\ \text{faces}} \hat{\alpha}_f A_f \mathbf{n} \tag{25}$$

where $\mathbf{n}$ is the outward-pointing normal vector at each face bounding the given cell, and $\hat{\alpha}_f$ is an approximate value obtained either from simple averaging of the cell neighbor values (cell-based

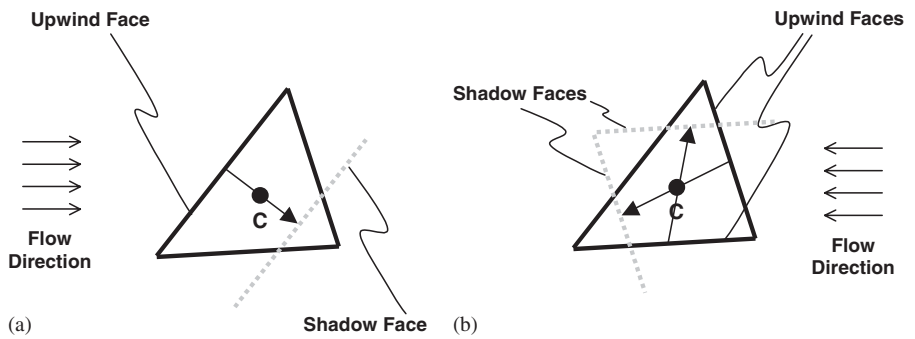

Figure 3. Illustration of shadow faces projected from upstream bounding faces, used to apply limiting constraint on the weighting parameter W in each cell. Shown are the cases of: (a) one and (b) two upwind/shadow face pairs, respectively.

DOI: 10.1002/fld

gradient computation) or averaging of the nodal values on the face (node-based gradient computation [18]).

On unstructured triangular and tetrahedral meshes, however, direct use of the Green–Gauss estimation of the gradient may result in a local 'inversion' of the interface orientation and degradation of solution accuracy. This behavior is eliminated by introducing an upwind-weighted gradient to be used in Equation (18), obtained as a volumetric-flow-rate-weighted average of the Green–Gauss gradients in upstream neighbor cells:

$$(\nabla\alpha)_C = \frac{\sum_{f:\dot{Q}_f<0} \dot{Q}_f (\nabla\alpha)_{GG,\mathrm{U}}}{\sum_{f:\dot{Q}_f<0} \dot{Q}_f} \tag{26}$$

Here the Green–Gauss gradient in each upstream cell, obtained via Equation (25), is denoted by $(\nabla\alpha)_{GG,\mathrm{U}}$. It has also been found that node-based computation [18] of the Green–Gauss gradients yields superior results on unstructured meshes versus cell-based gradient computation.

It is useful to compare and contrast the new scheme with existing high-resolution methods. The major similarity is the use of compressive downwind differencing to prescribe the face values of the volume fraction, introduced through the maximization of the weight function W in each cell. Likewise, the face values are limited to prevent over and undershoot that violates physical constraints. The fundamental difference lies in the manner with which the downwind differences are modified to prevent spurious behavior in the region of the discontinuity. The original VOF method [1] used simple switching between the compressive scheme and an upwind-biased scheme, while more recent methods [5–7], including the HRIC scheme outlined above, use a continuous blending parameter, which is a function of the angle between the interface and the control volume face. The BGM method proposed here follows a substantially different approach by considering only the net outward volume fraction flux for any given computational cell and ensuring that the net flux for all downstream faces is equivalent to the value obtained with (pure) upwind differencing. In this sense, the new method relies on cell-based flux limiting, rather than the face-based limiting that is employed in other schemes.

4. DEMONSTRATION TEST CASES

In order to highlight the capability of the new scheme, the solution of the volume fraction equation was first obtained for several prescribed velocity fields. Steady-state simulations were performed to determine the volume fraction distribution given by Equation (6). For all of the cases considered in this section, the interface is convected along the flow streamline, and the exact solution is easily determined for comparison purposes.

4.1. Two-dimensional test cases

Initial tests were performed on a 2-D square domain. Two meshes were constructed: a 100×100 cell Cartesian mesh and a comparable unstructured triangular mesh containing 10 116 cells. Both are shown in Figure 4.

The first set of test cases examined simple convection of the VOF interface in a uniform velocity field. Simulations were performed on the structured grid with the velocity oriented at a flow angle of 45, 26.56, and 14.04° relative to the x-axis. The inlet condition on the left ($x=0$) surface was

DOI: 10.1002/fld

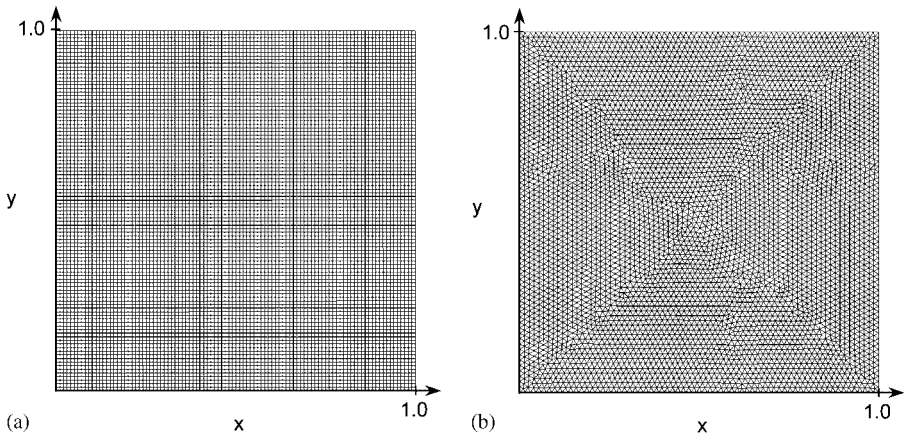

Figure 4. Illustration of initial 2-D test meshes: (a) 100×100 Cartesian mesh and (b) 10 116 cell triangular mesh.

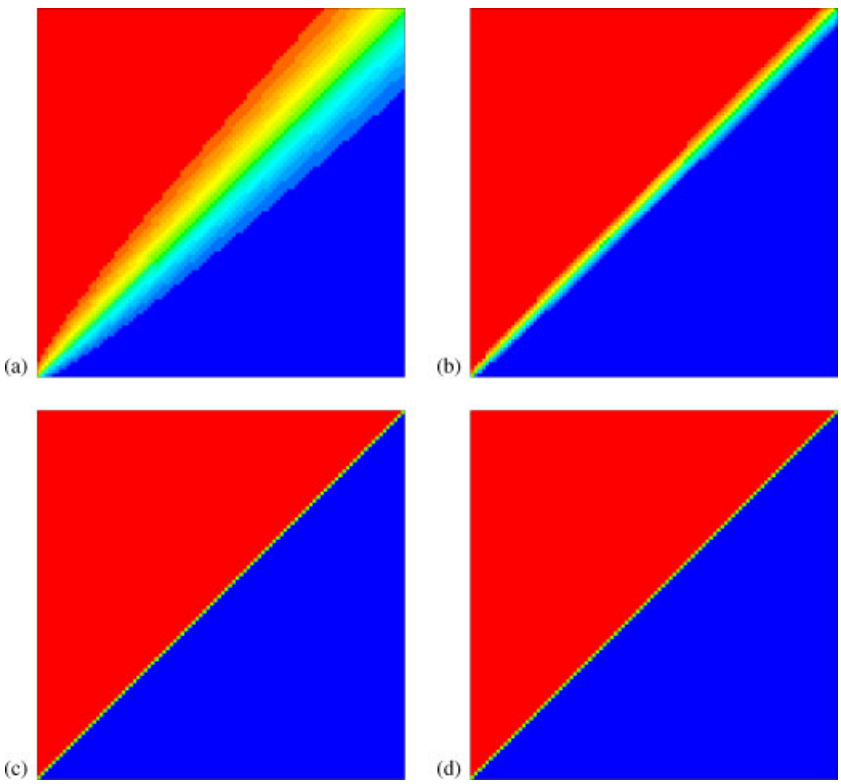

Figure 5. Non-smoothed contours of volume fraction for the 45° case; spatial discretization scheme: (a) first-order upwind; (b) second-order upwind; (c) HRIC; and (d) BGM.

DOI: 10.1002/fld

$\alpha = 1$ and the inlet condition on the bottom ($y = 0$) surface was $\alpha = 0$. The flow angles were chosen because they correspond to an interface slope of 1, 1/2, and 1/4, respectively. For each case, the computed volume fraction distributions were obtained using the first-order upwind scheme (Equation (10)), the second-order upwind scheme [12] (Equation (11)), the modified HRIC scheme [5] as incorporated into the FLUENT flow solver, and the new BGM scheme.

Figure 5 shows contours of the volume fraction for each of the discretization schemes, for the 45° flow direction. The contours are shown without any post-process smoothing in order to more clearly highlight the distribution of the volume fraction within computational cells in the vicinity of the interface. The excessive dissipation of the first-order upwind scheme is apparent. The second-order upwind scheme shows some improvement, but the results using both the HRIC and the BGM scheme are considerably less dissipative and better able to preserve the interface discontinuity throughout the domain. Figure 6 shows similar contours as for the 26.56° case; however, only the results from the HRIC and BGM schemes are shown. The discontinuity is once more well resolved by both; however, it is evident that the BGM scheme better preserves the interface discontinuity. This fact is highlighted in Figure 7, which shows a close-up view of volume fraction contours in the lower left region of the domain superimposed with the exact solution for the interface trajectory. For the BGM scheme, the only cells with values of the volume fraction not equal to zero or one are cells that contain the exact interface trajectory. In contrast, the HRIC scheme shows some dissipative behavior, with the volume fraction discontinuity being smeared over several cells in the vicinity of the interface. Figure 8 shows the non-smoothed contours for the remaining flow angle (14.04°), indicating similar behavior.

Plots of the volume fraction distribution for the three cases are shown in Figure 9 on the $y = 0.5$, 0.25, and 0.125 surfaces, respectively, for all but the first-order upwind scheme. It is apparent that the BGM scheme is able to capture the interface entirely within a minimum number of computational cells, while the second-order upwind and, to a lesser extent, the HRIC scheme show a slight 'diffusion' of the volume fraction over neighboring cells. This diffusive behavior becomes more severe as the flow angle becomes more aligned with the x-direction grid lines of the computational mesh. For the HRIC scheme this is presumably due to the increased weighting of the upwind-biased component as the interface orientation becomes more orthogonal to the y-direction grid lines.

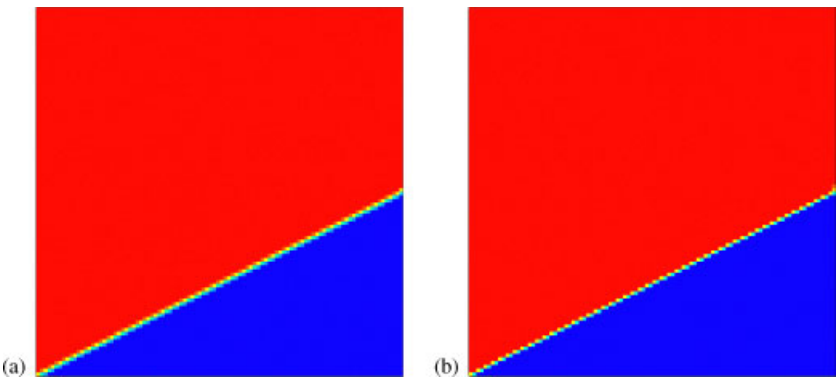

Figure 6. Non-smoothed contours of volume fraction for the 26.56° case; discretization scheme: (a) HRIC and (b) BGM.

DOI: 10.1002/fld

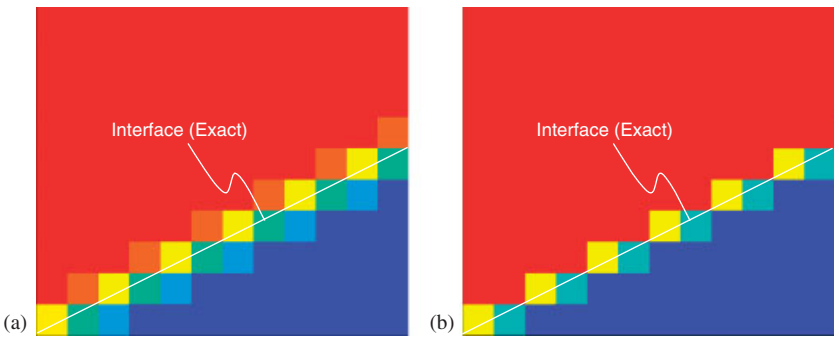

Figure 7. Close-up view of non-smoothed volume fraction contours for the 26.56° case using (a) the HRIC scheme and (b) the BGM scheme. It is apparent that the BGM scheme restricts the predicted location of the interface only to those cells that contain the (exact) interface location, while the HRIC scheme shows some smearing in the interface region.

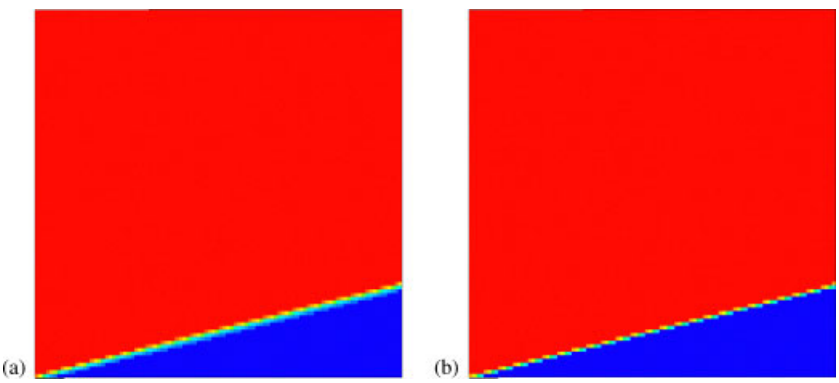

Figure 8. Non-smoothed contours of volume fraction for the 14.04° case; discretization scheme: (a) HRIC and (b) BGM.

The predicted volume fraction distribution on the unstructured mesh (Figure 4(b)) is shown only for the HRIC scheme and the BGM scheme in Figure 10. Results are shown for the case of 45° flow angle. It is apparent that both schemes show similar behavior on either a structured or an unstructured mesh topology. As above, the new scheme indicates minimal numerical diffusion of the interface discontinuity.

Results were next obtained for the case of a non-uniform velocity field. Figures 11–13 show the performance of different schemes for a steady 2-D velocity field described by:

$$U = 1 \tag{27}$$

$$V = A\cos(2\pi\kappa x) \tag{28}$$

The exact path of the interface discontinuity crossing the point (0,0) is therefore described by:

$$y_{\text{interface}} = \frac{A}{2\pi\kappa}\sin(2\pi\kappa x) \tag{29}$$

DOI: 10.1002/fld

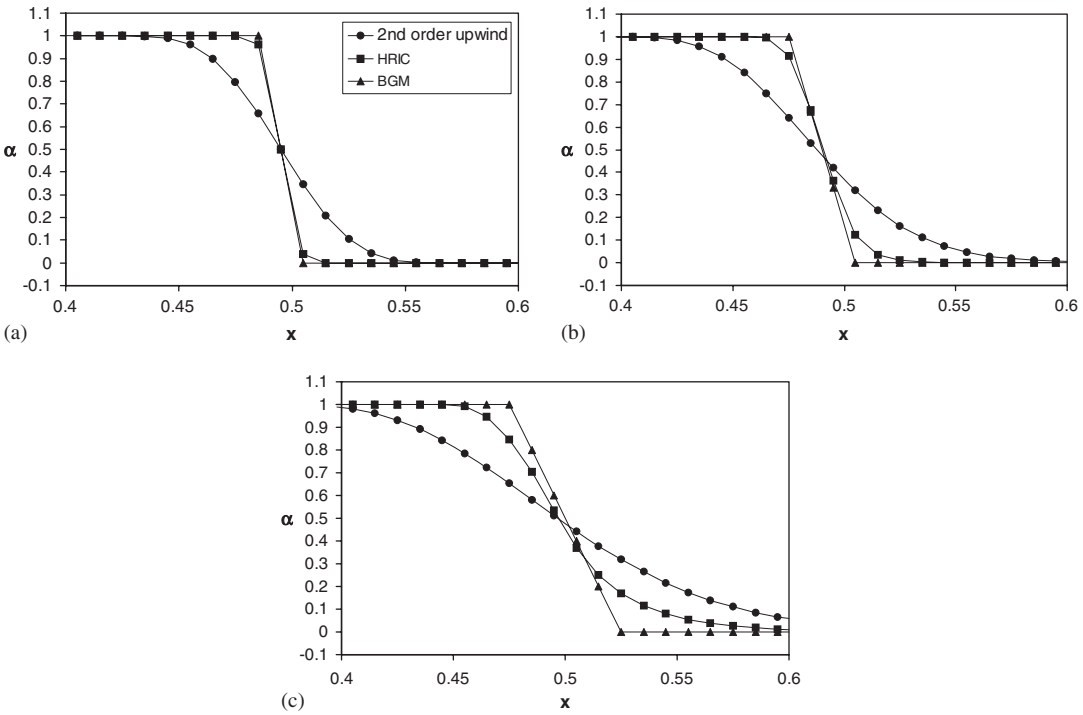

Figure 9. Computed volume fraction distribution for uniform velocity test cases on structured grid. Flow angle: (a) 45°; (b) 26.56°; and (c) 14.04°.

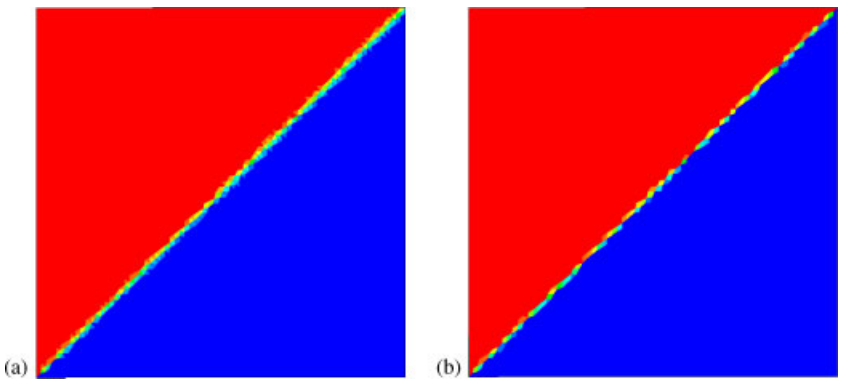

Figure 10. Non-smoothed contours of volume fraction for the 45° case on unstructured (triangular) mesh; discretization scheme: (a) HRIC and (b) BGM.

For these cases, the volume fraction inlet condition was applied at the left ($x=0$) boundary, with $\alpha=0$ in the region $y<0.5$, and $\alpha=1$ for $y>0.5$. The HRIC and BGM schemes were used to obtain results for $\kappa=2.5$, 5, and 10, representing successively smaller wavelengths of the sinusoidal interface path.

DOI: 10.1002/fld

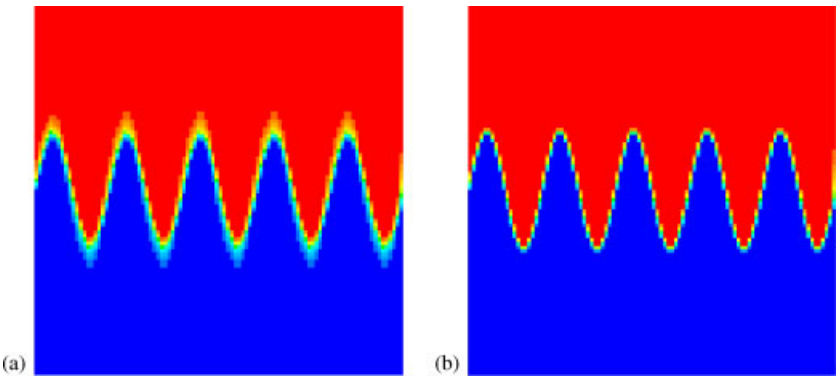

Figure 11. Non-smoothed contours of volume fraction for sinusoidally convected interface, $\kappa = 5$. Results are obtained using (a) HRIC scheme and (b) BGM scheme.

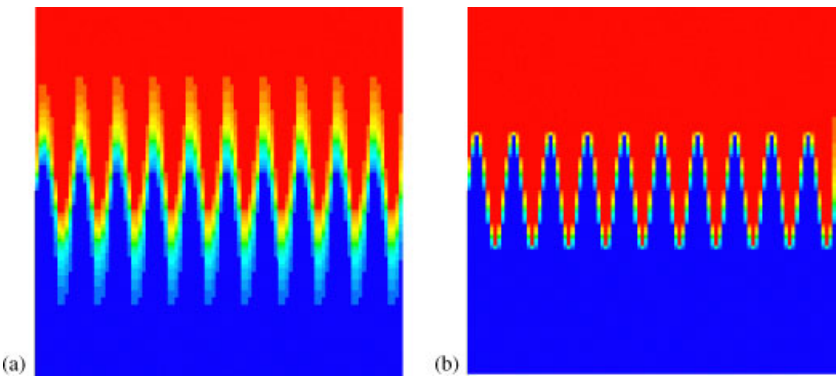

Figure 12. Non-smoothed contours of volume fraction for sinusoidally convected interface, $\kappa = 10$. Results are obtained using (a) HRIC scheme and (b) BGM scheme.

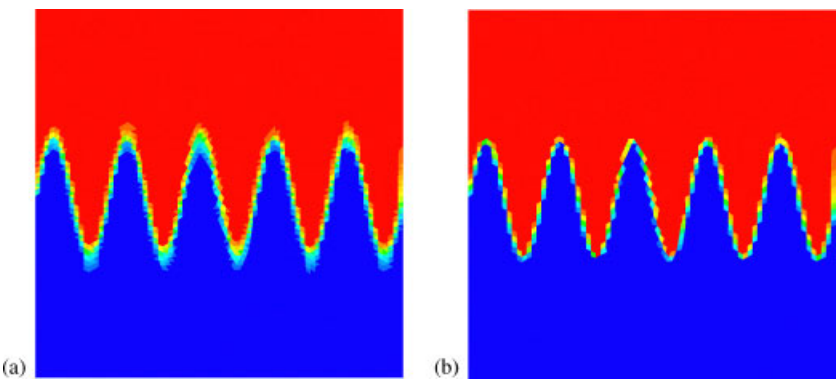

Figure 13. Non-smoothed contours of volume fraction for sinusoidally convected interface on unstructured mesh, $\kappa = 5$. Results are shown using (a) HRIC scheme and (b) BGM scheme.

DOI: 10.1002/fld

Figure 11 shows the results on the structured mesh for $\kappa=5$. Both the numerical schemes are able to preserve the interface discontinuity with a high degree of precision, though some level of diffusion is apparent in the results with the HRIC scheme. As the wavelength decreases (Figure 12), it is clear that the BGM scheme is better able to preserve the discontinuity and prevent smearing of the volume fraction contours over a large number of computational control volumes. Finally, the new scheme is compared with the HRIC scheme for the case of a sinusoidally varying velocity field using the unstructured mesh topology shown in Figure 4(b). The result for the case of $\kappa=5$ is shown in Figure 13. Similar to the results obtained on the structured mesh, the BGM method indicates minimal artificial diffusion of the phase interface.

4.2. Three-dimensional test cases

Two 3-D test cases are examined here. The first is convection of a round phase profile in a vortical flow field. This case is used to investigate the ability of the scheme to accurately resolve the phase interface for a long period of time with negligible artificial diffusion on an unstructured mesh, and to investigate the spatial convergence properties of the new scheme. The second test case is convection of a 'notched disk' phase profile [19] in a vortical flow field, in order to demonstrate the ability of the scheme to resolve a complex interface shape with minimal diffusion. Several other test cases have been previously reported that qualitatively demonstrate the performance of the new scheme on unstructured 3-D meshes [20].

The round phase profile investigated here was convected in a velocity field with uniform axial (z) velocity and a swirl component with uniform angular velocity about $r=0$. The phase profile had a diameter D, and was centered at $r=0$. The mesh consisted of an unstructured 2-D plane of diameter $2D$, extruded $40D$ in the axial direction. The swirl velocity was chosen such that one complete rotation occurred within each $10D$ of axial distance, resulting in 4 total rotations of the phase profile within the domain.

Three meshes were investigated, each with 200 cells in the axial direction, and varying levels of refinement in the transverse directions. The total number of cells was 37 600, 149 600, and 606 800 for the coarse, medium, and fine meshes, respectively. Each is illustrated in Figure 14.

Non-smoothed volume fraction contours are shown in Figure 15 for the coarse and fine mesh cases. As for the 2-D cases above, it is apparent that the BGM scheme is able to preserve the

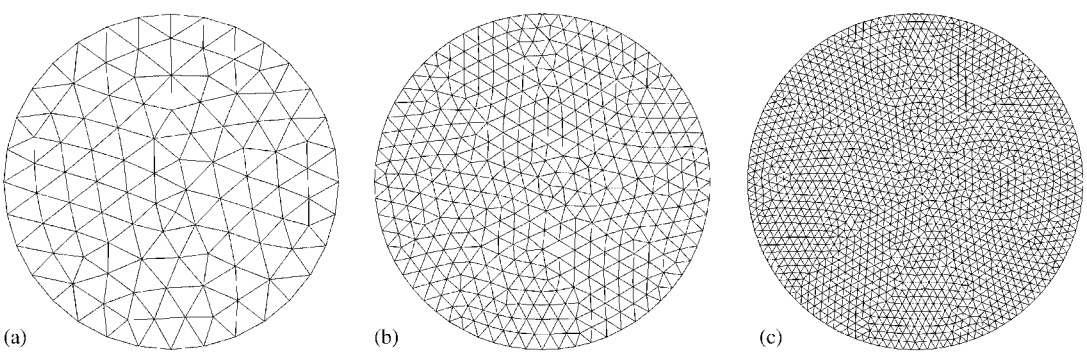

Figure 14. Inlet plane mesh for round phase profile test case: (a) coarse mesh; (b) medium mesh; and (c) fine mesh.

DOI: 10.1002/fld

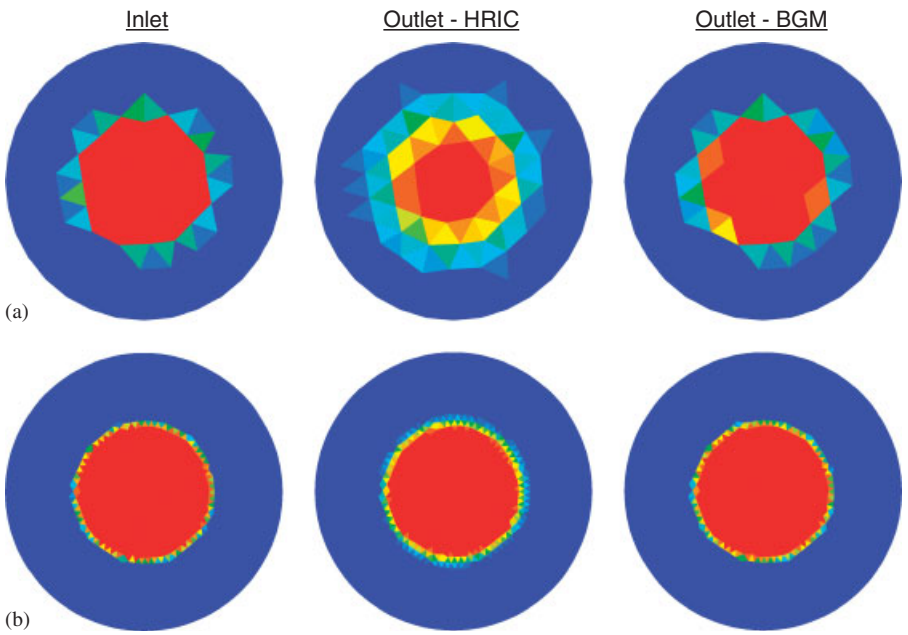

Figure 15. Non-smoothed volume fraction contours on the inlet plane, and on the outlet plane using each of the two high-resolution schemes: (a) coarse mesh and (b) fine mesh.

interface discontinuity with minimal artificial diffusion. The BGM scheme is also apparently capable of convecting the interface for long periods of time with little dissipative error.

The spatial convergence behavior of the two schemes is shown in Table I. The error at the outlet plane was computed according to the following definition (cf. [6]):

$$E = \frac{\sum_{f:\text{outlet}} |\alpha_f - \alpha_{\text{exact}}| \cdot A_f}{A_{\text{outlet}}} \tag{30}$$

where α_{exact} is the area-weighted average of the exact solution in each outlet face. Both the HRIC and the BGM schemes show an approximately first-order convergence rate. It has been previously pointed out that this behavior is expected when the discretization scheme captures the interface over a finite number of cells regardless of the mesh density, as the error can at best be reduced in proportion to the reduction in the characteristic cell width [6].

Both the high-resolution discretization schemes considered here are formally conservative. Computed volume fraction conservation for the two schemes is shown in Table II. The imbalance between the inlet and outlet flow rate is normalized by the net flow rate of volume fraction into the domain. The global imbalance is negligibly small for each of the two schemes, as expected.

The notched disk, known as Zalesak's Problem [19], represents a standard test case for evaluation of two-phase algorithms. As implemented here, the notched disk profile was convected in a prescribed 3-D velocity field, with uniform axial and angular velocity. The notched disk was prescribed with a diameter D, and centered at $r = 0.75D$. The notch had a width of $0.12D$ and a depth (into the disk) of $0.3D$. The unstructured inlet plane mesh and inlet phase profile are shown in Figure 16. The 3-D domain extended $1.5D$ in the radial and $10D$ in the axial direction. The

DOI: 10.1002/fld

Table I. Errors and order of convergence for round profile test case.

	HRIC		BGM	
Number of cells	Error	Order	Error	Order
37 600	2.4E−01		3.8E−02	
149 600	8.3E−02	1.55	2.1E−02	0.902
606 800	4.3E−02	0.945	8.5E−03	1.25

Table II. Global volume fraction imbalance for round profile test case.

Number of cells	HRIC Normalized imbalance	BGM Normalized imbalance
37 600	3.8E−05	5.0E−05
149 600	9.3E−05	6.7E−06
606 800	2.5E−05	1.1E−05

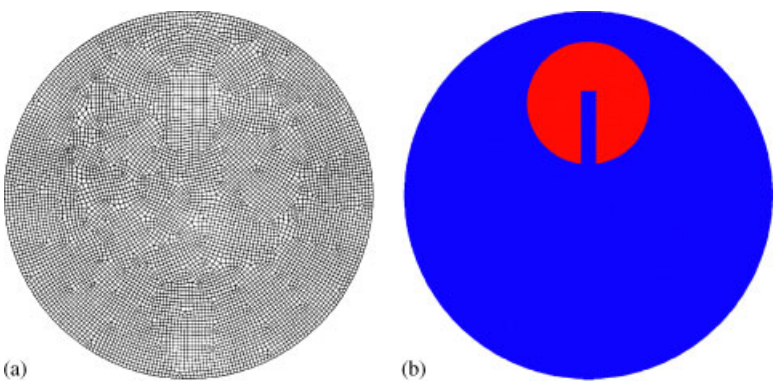

Figure 16. Inlet plane mesh (a) and inlet phase profile (b) for the notched-disk test case.

mesh contained 200 cells in the axial direction and 1.6 million cells overall. The angular velocity was chosen such that the disk made one complete revolution within the computational domain.

The results for this case using the BGM scheme are shown in Figure 17. Non-smoothed volume fraction contours are shown at one-fourth, one-half, three-fourths, and full revolution. The notched disk profile is maintained through the revolution, and very little dissipation of the interface is apparent. The sharp corners of the interface are slightly rounded after one complete rotation; however, this rounding effect is very small, and is known to occur to some degree for all interface-capturing discretization schemes. Figure 18 contrasts the outlet profile, after one rotation, using the HRIC and the BGM schemes. As in all previous test cases, BGM is less diffusive and more accurate than the HRIC scheme. The error for this case was computed using the definition in Equation (30), and was found to be 0.109 for the BGM scheme versus 0.157 for the HRIC scheme.

DOI: 10.1002/fld

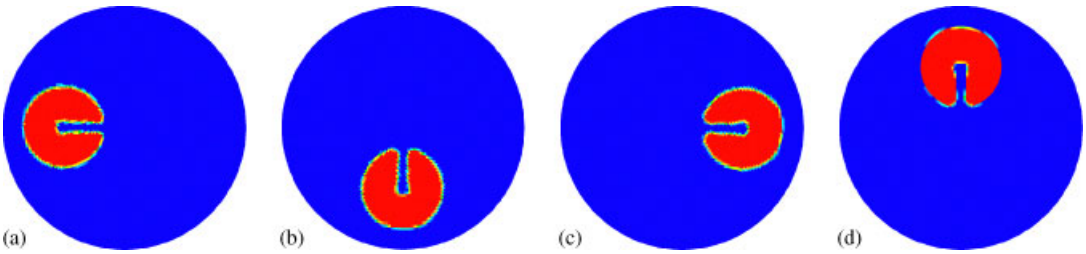

Figure 17. Predicted phase profile for the notched-disk test case at downstream locations corresponding to rotations of: (a) 90°; (b) 180°; (c) 270°; and (d) 360°.

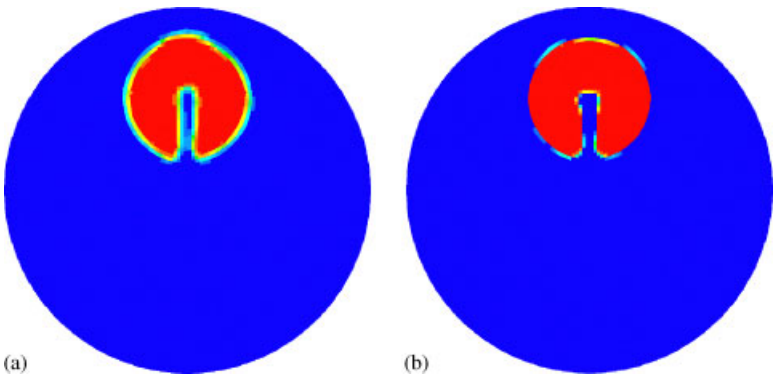

Figure 18. Outlet plane phase profile for the notched-disk test case for the two high-resolution discretization schemes: (a) HRIC and (b) BGM.

5. VALIDATION TEST CASES

In addition to the demonstration tests above, validation simulations were performed for which the overall flow solution included not only the solution of the volume fraction equation, but also the (coupled) solution of the velocity and pressure field. Two simple test cases were chosen, for which previously reported computational and/or experimental results are available for comparison purposes.

5.1. Low-Re oil/water flow in a two-dimensional channel

We first examine the two-phase flow of oil and water in a 2-D channel. This case was recently investigated numerically by Zubkov *et al.* [21] using an interface reconstruction VOF algorithm in combination with a very fine (801×101 cells) structured mesh. Two sets of simulations were performed, with the channel oriented at $+2°$ and $-2°$, with respect to horizontal. Results are presented here for the $+2°$ case only. The computational domain and meshes used in the present work are shown in Figure 19, with the channel height (H) as indicated. The overall computational domain extended from $x = 0$ to $x = 20$H, as in [21]. Four 2-D meshes were used: a coarse-structured mesh (200×20 cells), a refined-structured mesh (400×40 cells), a coarse-unstructured

DOI: 10.1002/fld

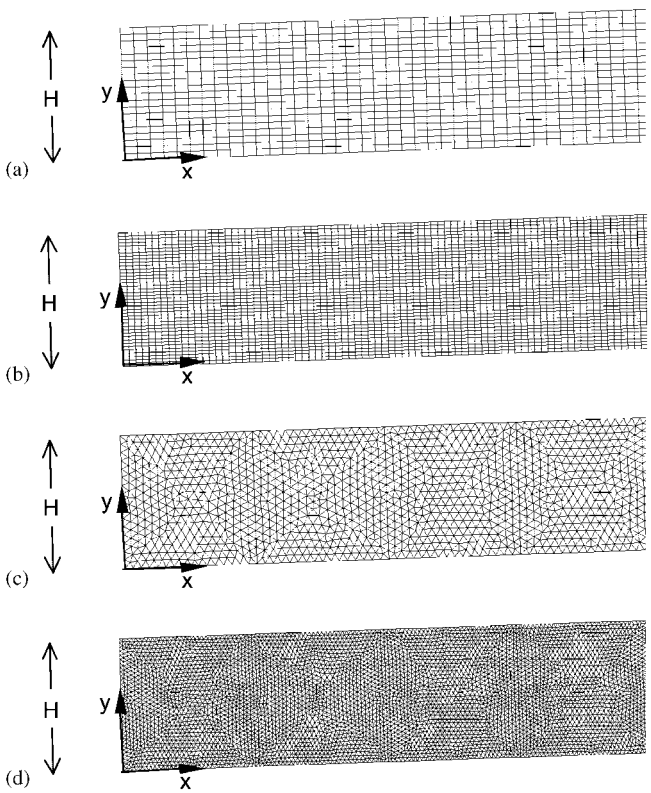

Figure 19. Computational domain and meshes used for oil/water flow test case. The four meshes used are: (a) coarse structured; (b) refined structured; (c) coarse unstructured; and (d) refined unstructured.

triangular mesh (11 464 total cells), and a refined-unstructured triangular mesh (45 856 total cells). The fluid phases were treated as incompressible, with constant properties for the water and oil: $\rho_{H_2O}=1000\,\mathrm{kg/m^3}$, $\mu_{H_2O}=0.001\,\mathrm{kg/m\,s}$, $\rho_{OIL}=790.5\,\mathrm{kg/m^3}$, $\mu_{OIL}=0.001551\,\mathrm{kg/m\,s}$. Average fluid properties were used to compute relevant dimensionless parameters: $\rho_{AVG}=1/2(\rho_{H_2O}+\rho_{OIL})$, $\mu_{AVG}=1/2(\mu_{H_2O}+\mu_{OIL})$. A uniform x-direction inlet velocity was applied at the inlet for both phases. Gravitational acceleration ($9.81\,\mathrm{m/s^2}$) was applied in the vertical (negative y) direction. Resulting dimensionless parameters were Froude number, $Fr=0.006$, and Reynolds number, $\mathrm{Re}=105$. The flow was therefore subcritical and laminar.

For the volume fraction equation, the primary phase was water ($\alpha=0$) and the secondary phase was oil ($\alpha=1$). The inlet was prescribed such that the lower half ($y/H<0.5$) was water and the upper half ($y/H>0.5$) was oil. The resulting steady flow field shows a stationary wave pattern near the domain inlet, with the oscillations reduced in the downstream direction until a fully developed two-phase channel flow is achieved, with the heavier fluid (water) moving with a lower mean velocity than the oil. The resulting volume fraction contours are shown for the structured and unstructured coarse meshes in Figure 20. The structured mesh results in Figure 20(a, b) demonstrate the tendency of the new discretization scheme to maintain the resolution of the phase interface within a minimum number of computational cells. By comparison, the HRIC scheme shows a

DOI: 10.1002/fld

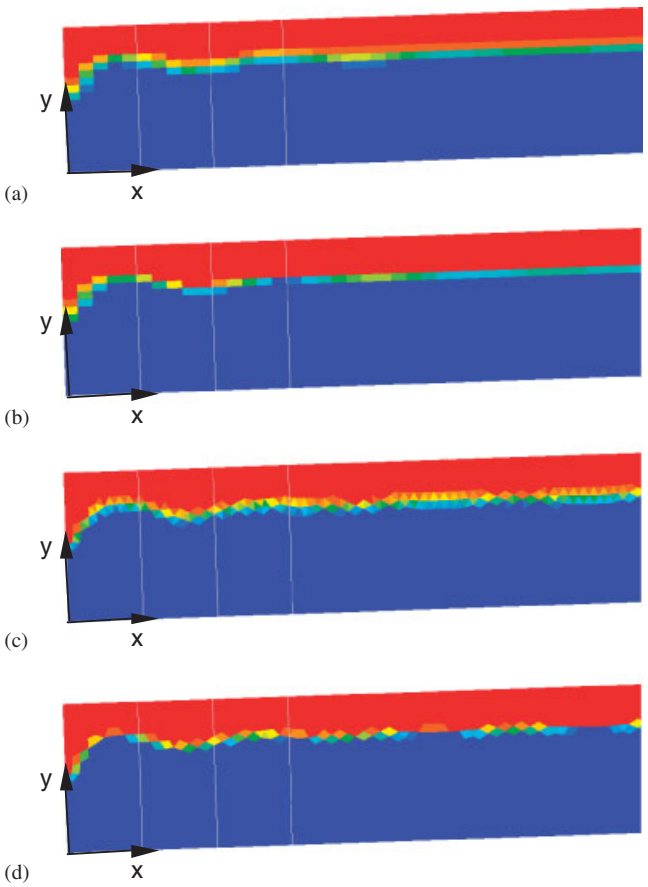

Figure 20. Non-smoothed contours of volume fraction for oil/water flow test case on coarse meshes: (a) HRIC scheme, structured mesh; (b) BGM scheme, structured mesh; (c) HRIC scheme, unstructured mesh; and (d) BGM scheme, unstructured mesh.

similar interface location, but a greater level of dissipation in the vicinity of the discontinuity. The same behavior is shown for the unstructured mesh results shown in Figure 20(c, d). Similar results were observed for the refined mesh cases. The key point is that the new discretization scheme yields results for volume fraction similar to those shown in the previous section when coupled to the continuity and momentum equations.

The computed volume fraction distribution is compared with the reference results [21] in Figure 21, which contains plots of volume fraction versus normalized y-coordinate at a measurement location corresponding to $x/H = 0.5$. Four separate plots are presented corresponding to the four different meshes used. On each plot is shown the reference result and the results obtained with the HRIC and BGM schemes. It is apparent that both schemes show excellent agreement with the reference, and in general the agreement improves with increasing mesh resolution, as expected. The results highlight the ability of the new volume fraction discretization to yield accurate results for a simple two-phase flow simulation, while maintaining very high resolution of the phase interface.

DOI: 10.1002/fld

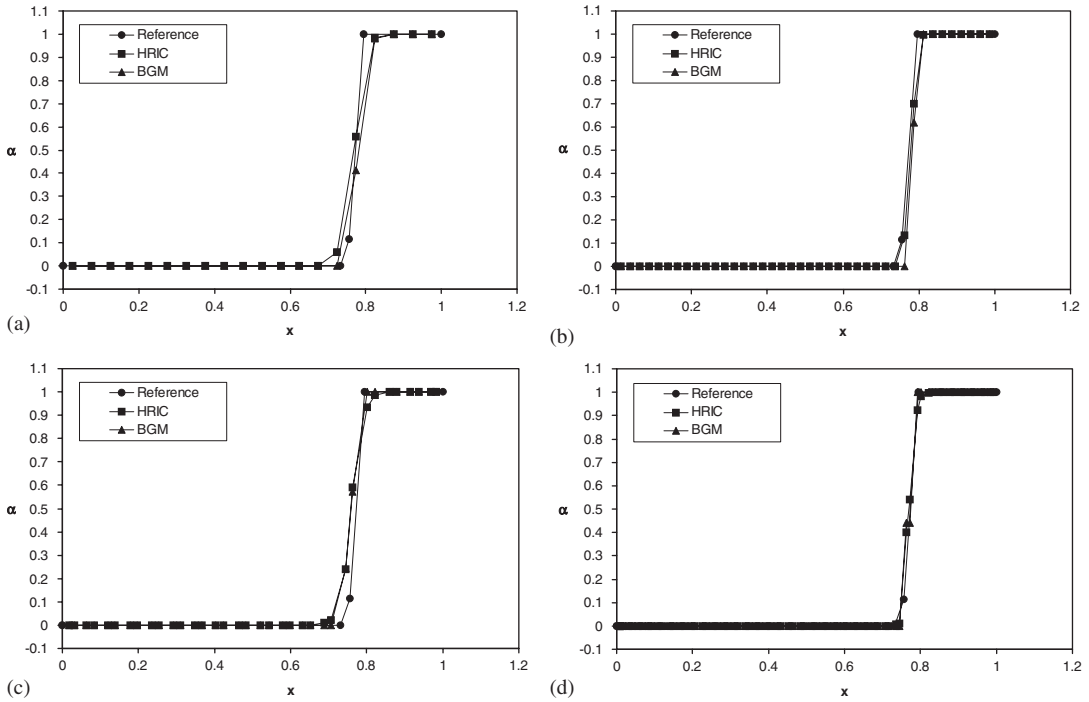

Figure 21. Computed volume fraction profiles at $x/H=0.5$: (a) coarse-structured mesh; (b) refined-structured mesh; (c) coarse-unstructured mesh; and (d) refined-unstructured mesh.

5.2. *Free-surface flow over submerged bottom topography*

Finally, the performance of the discretization scheme is evaluated for a simple free-surface flow. The test case is a contoured bottom topography in 2-D channel flow, and results are compared with available experimental data [22]. This case has been used previously for evaluation of surface-tracking free-surface algorithms [23]. As above, solutions were obtained on several meshes, including a coarse-structured, refined-structured, and one unstructured mesh, shown in Figure 22. A uniform inlet velocity of 1.985 m/s was applied at the upstream inlet to the domain, and the VOF simulation was performed with air as the primary phase ($\alpha=0$) and water as the secondary phase ($\alpha=1$). Material properties were chosen to match experimental values: $\rho_{\mathrm{AIR}}=1.225\,\mathrm{kg/m^3}$, $\mu_{\mathrm{AIR}}=1.79\times10^{-5}\,\mathrm{kg/m\,s}$, $\rho_{\mathrm{H_2O}}=1000\,\mathrm{kg/m^3}$, $\mu_{\mathrm{H_2O}}=0.001\,\mathrm{kg/m\,s}$. The overall domain height was 0.48 m, and the inlet depth of the water was 0.09545 m. The inlet Reynolds number based on depth was 1.9×10^5. Standard gravitational acceleration was applied in the negative y direction. The flow was therefore supercritical, with $Fr=2.05$.

Results are once more presented comparing the new BGM discretization scheme with the modified HRIC scheme. Figure 23 shows contours of volume fraction using both schemes, in the vicinity of the contoured bottom, for the coarse-structured mesh. Because the flow is supercritical, a single elevated surface region forms over the topography. As before, it is apparent that the new scheme is able to represent the interface discontinuity across a minimum of computational cells. The free surface, which is oriented primarily horizontally, is resolved within one cell in the y direction.

DOI: 10.1002/fld

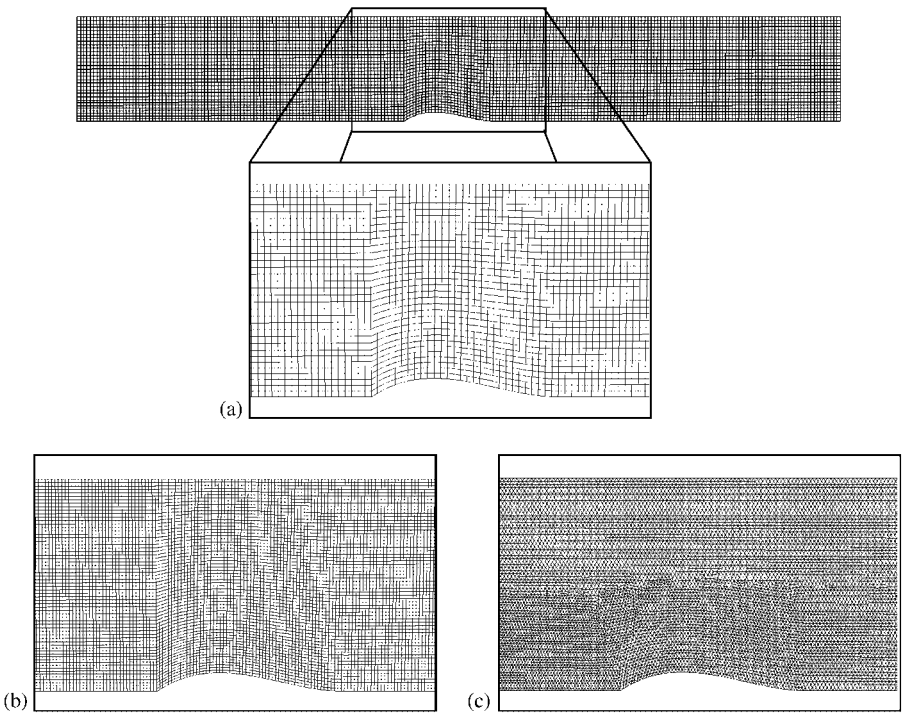

Figure 22. Computational domain and mesh topologies used for free-surface test case. The region of near submerged topography is shown for the: (a) coarse-structured mesh; (b) refined-structured mesh; and (c) unstructured mesh.

In contrast, the HRIC scheme resolves the free surface over one to three computational cells, depending on the location. Identical behavior was observed on the refined-structured mesh and is shown for the unstructured mesh in Figure 24.

The predicted location of the free surface is plotted in Figure 25 and compared with experimental data [22]. The free-surface location is defined as the location at which the volume fraction α equals 0.5. It is clear that the free surface is well predicted for each combination of mesh and discretization scheme. In fact, results with the more dissipative second-order upwind scheme showed essentially identical behavior, though the free surface was found to be smeared over a large number of computational cells. This result helps to explain the ability of existing methods to provide acceptable levels of accuracy for a number of two-phase flow problems (cf. [8, 9, 14, 15]). The contribution of the new methodology lies in the ability to not only accurately predict the location of the interface, but also to resolve the interface within a minimum number of finite mesh cells.

6. SUMMARY AND CONCLUSIONS

The goal of this paper has been to present a new discretization methodology for application to VOF simulations of multi-phase flows. The new method is based on an interface-capturing approach, in which the phase discontinuity is resolved implicitly by the spatial discretization scheme rather than

DOI: 10.1002/fld

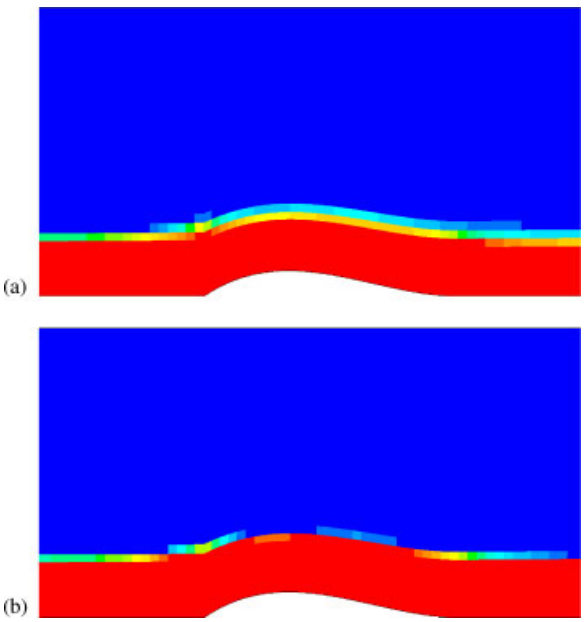

Figure 23. Non-smoothed contours of volume fraction for supercritical free-surface flow on coarse-structured mesh, obtained with: (a) HRIC scheme and (b) BGM scheme.

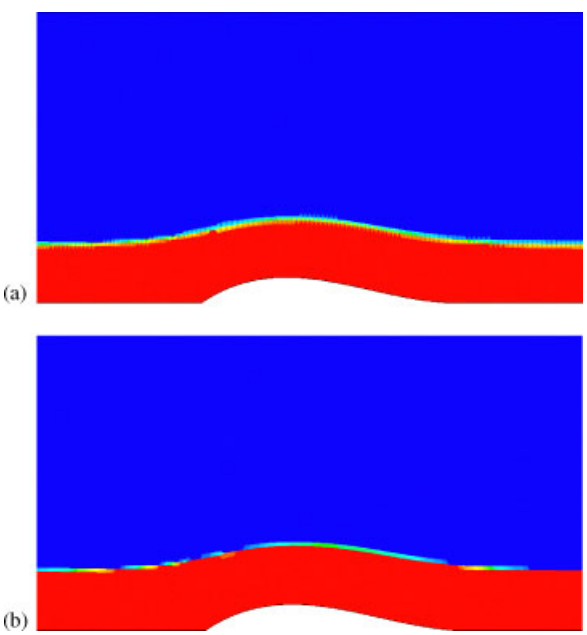

Figure 24. Non-smoothed contours of volume fraction for supercritical free-surface flow on unstructured mesh, obtained with: (a) HRIC scheme and (b) BGM scheme.

DOI: 10.1002/fld

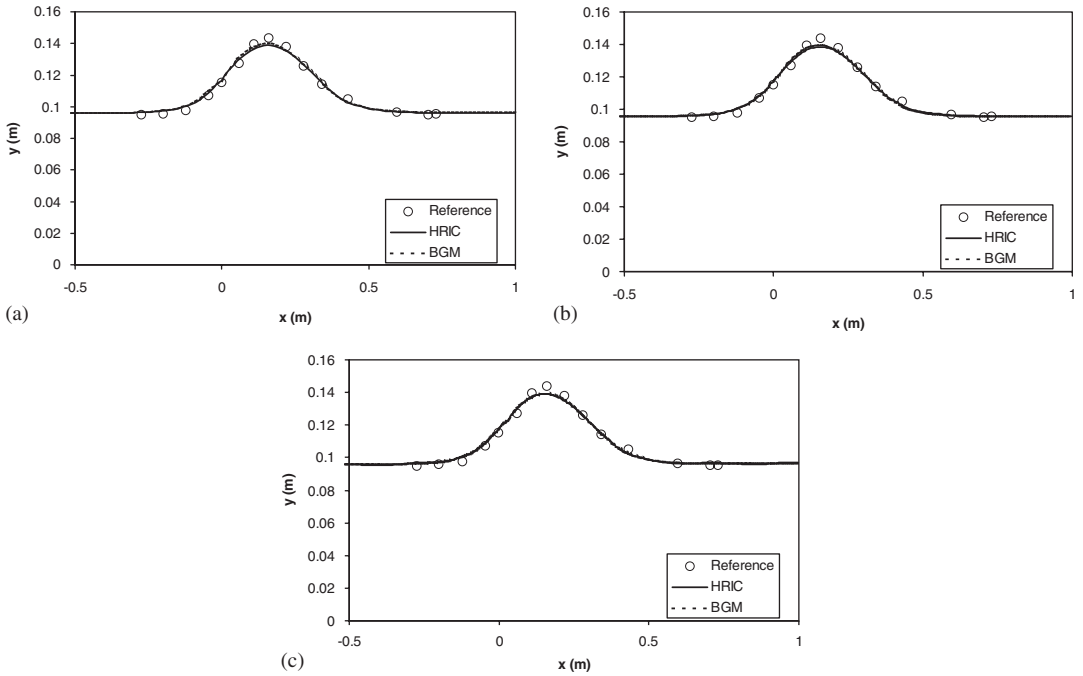

Figure 25. Location of free surface for submerged bottom topography test case, defined by location at which $a = 0.5$. Results are shown for the: (a) coarse-structured mesh; (b) refined-structured mesh; and (c) unstructured mesh.

explicitly reconstructed. To date, this approach has been most commonly implemented using high-resolution discretization schemes that rely on compressive downwind differencing to minimize artificial diffusion, blended with upwind differences in order to preserve physically correct behavior in the region of the interface. The resulting schemes can therefore be thought to represent an *ad hoc* optimization between dissipation and stability.

The new scheme relies on an alternative formulation that makes use of downwind differencing, but maintains stability in the vicinity of the interface by incorporating a flux component that preserves a net upwind flux prescription for the sum of the downstream faces of each computational control volume. The scheme is therefore based on cell-based rather than face-based limiting.

Results have been presented for simple demonstration test cases and for more realistic validation test cases. The former highlight the capability of the new scheme to preserve the phase interface with a high level of accuracy, by confining the volume fraction to values between zero and one within a minimum number of cells in the vicinity of the interface. In contrast, existing methods tend to show some distribution of the variation in volume fraction over several cells near the interface, particularly in those instances where the mesh lines are nearly orthogonal to the interface path, as it is in these cases that the schemes tend to more heavily weight the upwind differencing component. The demonstration cases show the ability of the new scheme to yield highly resolved predictions of the discontinuity on both structured and unstructured meshes.

The validation cases were likewise chosen to highlight the ability of the new scheme to accurately resolve the interface, and include oil–water flow in a 2-D channel [21], and free-surface air–water

DOI: 10.1002/fld

flow in a 2-D channel with a contoured bottom [22]. Comparison with available reference data shows that the new scheme performs at least as well as existing methods in predicting the overall location of the interface, while demonstrating the ability to minimize diffusion of the interface without evidencing any non-physical wrinkling.

Future work will include application of the new scheme to more complex steady-state flows as well as time-dependent problems. The basis of the spatial discretization scheme outlined here will be extended to a coupled time–space methodology, which will allow similar behavior in terms of accuracy and stability as the steady-state implementation, while preserving conservation in both space and time.

ACKNOWLEDGEMENTS

This work was performed with partial funding from the National Science Foundation, under Grant No. EPS-0556308. The authors gratefully acknowledge the support. We would like to thank Fluent, Inc. for their software support and for the collaborative efforts of Dr Dipankar Choudhury and Dr Davor Cokljat. The authors also appreciate the continued support of the administrative and technical personnel of the Mississippi State University High Performance Computing Collaboratory (HPC^2).

REFERENCES

1. Hirt CW, Nichols BD. Volume of fluid method for dynamics of free boundaries. *Journal of Computational Physics* 1981; **39**:201–225.
2. Noh WF, Woodward PR. In *SLIC* (*Simple Line Interface Calculation*), Van der Vooren AI, Zandbergen PJ (eds). Lecture Notes in Physics, vol. 59. Springer: New York, 1976; 330–340.
3. Rider WJ, Kothe DB. Reconstructing volume tracking. *Journal of Computational Physics* 1998; **141**:112–152.
4. Leonard BP. The ULTIMATE conservative difference scheme applied to unsteady one-dimensional advection. *Computer Methods in Applied Mechanics and Engineering* 1991; **88**:17–74.
5. Muzaferija S, Peric M, Sames P, Schellin T. A two-fluid Navier–Stokes solver to simulate water entry. *Proceedings of 22nd Symposium on Naval Hydrodynamics*, Washington, DC, 1998; 638–651.
6. Ubbink O, Issa RI. A method for capturing sharp fluid interfaces on arbitrary meshes. *Journal of Computational Physics* 1999; **153**:26–50.
7. Dendy ED, Padial-Collins NT, VanderHayden WB. A general-purpose finite-volume advection scheme for continuous and discontinuous fields on unstructured grids. *Journal of Computational Physics* 2002; **180**:559–583.
8. Rhee SH, Makarov BP, Krishinan H, Ivanov V. Assessment of the volume of fluid method for free-surface wave flow. *Journal of Marine Science and Technology* 2005; **10**:173–180.
9. Rhee SH. Unstructured grid based Reynolds-averaged Navier–Stokes method for liquid tank sloshing. *Transactions of the ASME*: *Journal of Fluids Engineering* 2005; **127**:572–582.
10. Patankar SV. *Numerical Heat Transfer and Fluid Flow*. Hemisphere: Washington, DC, 1980.
11. *FLUENT 6.2.16 User's Guide*. Fluent, Inc.: Lebanon, NH, 2003.
12. Barth TJ, Jespersen D. The design and application of upwind schemes on unstructured meshes. *Proceedings of 27th AIAA Aerospace Sciences Meeting*, Reno, NV, 1989. AIAA Paper No. AIAA-89-0366.
13. Hardt S. An extended volume-of-fluid method for micro flows with short-range interactions between fluid interfaces. *Physics of Fluids* 2005; **17**:100601.
14. Brennan M. CFD simulations of hydrocyclones with an air core: comparison between large eddy simulations and a second moment closure. *Chemical Engineering Research and Design* 2006; **84**:495–505.
15. Nguyen AV, Evans GM. Computational fluid dynamics modelling of gas jets impinging onto liquid pools. *Applied Mathematical Modelling* 2006; **30**:1472–1484.
16. Taha T, Cui ZF. CFD modelling of slug flow in vertical tubes. *Chemical Engineering Science* 2006; **61**:676–687.
17. Lafaurie B, Nardone C, Scardovelli R, Zaleski S, Zanetti G. Modelling merging and fragmentation in multiphase flows with SURFER. *Journal of Computational Physics* 2002; **113**:134–147.
18. Holmes DG, Connell SD. Solution of the 2-D Navier–Stokes equations on unstructured adaptive grids. *Proceedings of AIAA 9th Computational Fluid Dynamics Conference*, Buffalo, NY, 1989. AIAA Paper No. 89-1932.

DOI: 10.1002/fld

19. Zalesak ST. Fully multidimensional flux-corrected transport algorithms for fluids. *Journal of Computational Physics* 1979; **31**:335–362.
20. Walters DK. Application of high-resolution spatial discretization schemes to volume-of-fluid simulations on three-dimensional unstructured meshes. *Proceedings of ASME International Mechanical Engineering Congress and Exposition*, Seattle, WA, 2007. ASME Paper No. IMECE2007-43965.
21. Zubkov PT, Serebryakov VV, Son EE, Tarasova EN. Steady-state flow of two viscous immiscible incompressible fluids in a plane channel. *High Temperature* 2005; **43**:769–774.
22. Cahouet J. Etude numerique et experimentale du probleme bidimensionel de la resistance de vagues non-lineare. *Ph.D. Thesis*, ENSTA, Paris, 1984.
23. Tzabiras GD. A numerical investigation of 2D, steady free surface flows. *International Journal for Numerical Methods in Fluids* 1997; **25**:567–598.

DOI: 10.1002/fld